

REPORT DOCUMENTATION PAGE

Form Approved OMB NO. 0704-0188

The public reporting burden for this collection of information is estimated to average 1 hour per response, including the time for reviewing instructions, searching existing data sources, gathering and maintaining the data needed, and completing and reviewing the collection of information. Send comments regarding this burden estimate or any other aspect of this collection of information, including suggestions for reducing this burden, to Washington Headquarters Services, Directorate for Information Operations and Reports, 1215 Jefferson Davis Highway, Suite 1204, Arlington VA, 22202-4302. Respondents should be aware that notwithstanding any other provision of law, no person shall be subject to any penalty for failing to comply with a collection of information if it does not display a currently valid OMB control number.  
PLEASE DO NOT RETURN YOUR FORM TO THE ABOVE ADDRESS.

|  |                  |                                |   |   |  |
|--|------------------|--------------------------------|---|---|--|
| 1. REPORT DATE (DD-MM-YYYY)<br>20-12-2008  |                  | 2. REPORT TYPE<br>Final Report |   | 3. DATES COVERED (From - To)<br>16-May-2005 - 15-May-2008 |  |
| 4. TITLE AND SUBTITLE<br>Final Report: Complexity-enabled sensor networks and photonic switching devices   |                  |                                | 5a. CONTRACT NUMBER<br>W911NF-05-1-0228 |   |  |
|  |                  |                                | 5b. GRANT NUMBER                        |   |  |
|  |                  |                                | 5c. PROGRAM ELEMENT NUMBER<br>611102    |   |  |
| 6. AUTHORS<br>D.J. Gauthier  |                  |                                | 5d. PROJECT NUMBER                      |   |  |
|  |                  |                                | 5e. TASK NUMBER                         |   |  |
|  |                  |                                | 5f. WORK UNIT NUMBER                    |   |  |
| 7. PERFORMING ORGANIZATION NAMES AND ADDRESSES<br>Duke University<br>Office of Research Support<br>Duke University<br>Durham, NC 27705 -   |                  |                                |   | 8. PERFORMING ORGANIZATION REPORT NUMBER                  |  |
| 9. SPONSORING/MONITORING AGENCY NAME(S) AND ADDRESS(ES)<br>U.S. Army Research Office<br>P.O. Box 12211<br>Research Triangle Park, NC 27709-2211  |                  |                                |   | 10. SPONSOR/MONITOR'S ACRONYM(S)<br>ARO                   |  |
|  |                  |                                |   | 11. SPONSOR/MONITOR'S REPORT NUMBER(S)<br>47562-PH-DRI.17 |  |
| 12. DISTRIBUTION AVAILABILITY STATEMENT<br>Approved for Public Release, Federal Purpose Rights   |                  |                                |   |   |  |
| 13. SUPPLEMENTARY NOTES<br>The views, opinions and/or findings contained in this report are those of the author(s) and should not be construed as an official Department of the Army position, policy or decision, unless so designated by other documentation.  |                  |                                |   |   |  |
| 14. ABSTRACT<br>The researchers have demonstrated that a holistic, complexity-based design approach can lead to improved functionality or sensitivity of devices. They have developed two different types of devices, each of which is optimized for different applications: an opto-electronic chaotic oscillator that can be used as a building block for an intrusion detection network; and an ultra-low-light-level photonic switch for quantum information networks. Although these devices are quite different, they are both enabled by complexity. Their realization demonstrates that complexity can solve problems on two different scales: it offers a new approach to creating a device that can be integrated into an existing system (micro scale) on the one hand, and |                  |                                |   |   |  |
| 15. SUBJECT TERMS<br>ultra-low-light-level nonlinear optics, opto-electronic oscillators, broadband chaos, transverse patterns, optical switching, chaotic sensor networks, time-delay differential equations, optical transistor  |                  |                                |   |   |  |
| 16. SECURITY CLASSIFICATION OF:  |                  | 17. LIMITATION OF ABSTRACT     |   | 15. NUMBER OF PAGES                                       |  |
| a. REPORT<br>U   | b. ABSTRACT<br>U | c. THIS PAGE<br>U              |   | 19a. NAME OF RESPONSIBLE PERSON<br>Daniel Gauthier        |  |
|  |                  |                                |   | 19b. TELEPHONE NUMBER<br>919-660-2511                     |  |

## Report Title

Final Report: Complexity-enabled sensor networks and photonic switching devices

### ABSTRACT

The researchers have demonstrated that a holistic, complexity-based design approach can lead to improved functionality or sensitivity of devices. They have developed two different types of devices, each of which is optimized for different applications: an opto-electronic chaotic oscillator that can be used as a building block for an intrusion detection network; and an ultra-low-light-level photonic switch for quantum information networks. Although these devices are quite different, they are both enabled by complexity. Their realization demonstrates that complexity can solve problems on two different scales: it offers a new approach to creating a device that can be integrated into an existing system (micro scale) on the one hand, and that the functionality of an entire system can be entirely based on complexity (macro scale).

---

### List of papers submitted or published that acknowledge ARO support during this reporting period. List the papers, including journal references, in the following categories:

#### (a) Papers published in peer-reviewed journals (N/A for none)

A.M.C. Dawes, L. Illing, J.A. Greenberg, D.J. Gauthier, 'All-Optical Switching with Transverse Optical Patterns,' Phys. Rev. A 77, 013833 (2008).

J.A. Greenberg, M. Oria, A.M.C. Dawes, D.J. Gauthier, 'Absorption-Induced Trapping in an Anisotropic Magneto-optical Trap,' Opt. Express 15, 17699 (2007).

L. Illing, D.J. Gauthier, and J.N. Blakely, 'Controlling fast chaos in opto-electronic delay dynamical systems,' an invited chapter in Handbook of Chaos Control, 2nd Ed., E. Schöll, and H. G. Schuster, Eds. (WILEY-VCH Verlag GmbH & Co. KGaA, Weinheim, Germany, 2008), pp. 407-425.

**Number of Papers published in peer-reviewed journals:** 3.00

---

#### (b) Papers published in non-peer-reviewed journals or in conference proceedings (N/A for none)

**Number of Papers published in non peer-reviewed journals:** 0.00

---

#### (c) Presentations

A.M.C. Dawes and D.J. Gauthier, 'Transverse Patterns for All-Optical Switching,' Quantum Electronics and Laser Science 2008, San Jose, CA, May 5, 2008.

Z. Gao and D.J. Gauthier, 'Parameter-space study of an ultra-high frequency chaotic circuit with delayed feedback,' Dynamics Days 2008, Knoxville, TN, Jan. 3-6, 2008.

J.A. Greenberg, M. Oria, and D.J. Gauthier. 'Anisotropic MOT for Nonlinear Optical Studies', Atomic Physics Gordon Research Conference, Tilton School, NH, July 1-6, 2007.

A. M. C. Dawes and D. J. Gauthier, 'Using Transverse Patterns for All-Optical Switching,' Ninth Rochester Conference on Coherence & Quantum Optics (CQO9), Rochester, NY, June 10-13, 2007.

**Number of Presentations:** 4.00

---

#### Non Peer-Reviewed Conference Proceeding publications (other than abstracts):

**Number of Non Peer-Reviewed Conference Proceeding publications (other than abstracts):** 0

---

#### Peer-Reviewed Conference Proceeding publications (other than abstracts):

**(d) Manuscripts**

K.E. Callan, L. Illing, Z. Gao, D.J. Gauthier, and E. Schoell, 'Broadband chaos generated by an opto-electronic oscillator,' submitted for publication (2008).

A.M.C. Dawes, D.J. Gauthier, S. Schumacher, N.H. Kwong, R. Binder and A.L. Smirl, 'Transverse optical patters for ultra-low-light-level all-optical switching,' an invited article in Laser & Photonics Rev. (2008).

**Number of Manuscripts:** 2.00

**Number of Inventions:****Graduate Students**

| <u>NAME</u>            | <u>PERCENT SUPPORTED</u> |
|------------------------|--------------------------|
| Kristine Callan        | 0.75                     |
| Joel Greenberg         | 0.75                     |
| Andrew Dawes           | 0.25                     |
| <b>FTE Equivalent:</b> | <b>1.75</b>              |
| <b>Total Number:</b>   | <b>3</b>                 |

**Names of Post Doctorates**

| <u>NAME</u>            | <u>PERCENT SUPPORTED</u> |
|------------------------|--------------------------|
| <b>FTE Equivalent:</b> |                          |
| <b>Total Number:</b>   |                          |

**Names of Faculty Supported**

| <u>NAME</u>            | <u>PERCENT SUPPORTED</u> | National Academy Member |
|------------------------|--------------------------|-------------------------|
| Daniel Gauthier        | 0.04                     | No                      |
| <b>FTE Equivalent:</b> | <b>0.04</b>              |                         |
| <b>Total Number:</b>   | <b>1</b>                 |                         |

**Names of Under Graduate students supported**

| <u>NAME</u>            | <u>PERCENT SUPPORTED</u> |
|------------------------|--------------------------|
| <b>FTE Equivalent:</b> |                          |
| <b>Total Number:</b>   |                          |

**Student Metrics**

This section only applies to graduating undergraduates supported by this agreement in this reporting period

- The number of undergraduates funded by this agreement who graduated during this period: ..... 0.00
- The number of undergraduates funded by this agreement who graduated during this period with a degree in science, mathematics, engineering, or technology fields:..... 0.00
- The number of undergraduates funded by your agreement who graduated during this period and will continue to pursue a graduate or Ph.D. degree in science, mathematics, engineering, or technology fields:..... 0.00
- Number of graduating undergraduates who achieved a 3.5 GPA to 4.0 (4.0 max scale):..... 0.00
- Number of graduating undergraduates funded by a DoD funded Center of Excellence grant for Education, Research and Engineering:..... 0.00
- The number of undergraduates funded by your agreement who graduated during this period and intend to work for the Department of Defense ..... 0.00
- The number of undergraduates funded by your agreement who graduated during this period and will receive scholarships or fellowships for further studies in science, mathematics, engineering or technology fields: ..... 0.00

**Names of Personnel receiving masters degrees**

|  |                      |
|--|----------------------|
| <u>NAME</u><br>Kristine Callan<br>Joel Greenberg<br><b>Total Number:</b> | <br><br><br><b>2</b> |
|--|----------------------|

**Names of personnel receiving PHDs**

|   |                  |
|---|------------------|
| <u>NAME</u><br>Andrew Dawes<br><b>Total Number:</b> | <br><br><b>1</b> |
|---|------------------|

**Names of other research staff**

|  |  |
|--|--|
| <u>NAME</u><br>Marcos Oria<br><b>FTE Equivalent:</b><br><b>Total Number:</b> | <u>PERCENT SUPPORTED</u><br>0.18 No<br><b>0.18</b><br><b>1</b> |
|--|--|

**Sub Contractors (DD882)**

**Inventions (DD882)**



Over the duration of this grant, we have developed electronic and photonic chaotic elements that will form the basis of chaos-based sensor networks. In addition, we have developed and optimized a new method for ultra-low-light-level all-optical switching using transverse patterns. We are recognized as leaders in both of these areas and have been invited to write extensive review articles on both topics. Below, we highlight some of our accomplishments from this project.

## **I. Ultra-high-frequency chaotic elements**

### **I.A. Ultra-high-frequency chaos in a time-delay electronic device with band-limited feedback**

We conducted an experimental study of ultra-high-frequency chaotic dynamics generated in a delay-dynamical electronic device. It consists of a transistor-based nonlinearity, commercially-available amplifiers, and a transmission-line for feedback. The feedback is band-limited, allowing tuning of the characteristic time-scales of both the periodic and high-dimensional chaotic oscillations that can be generated with the device. We developed a model and used it to compare the experimentally observed Hopf-bifurcation of the steady-state to existing theory [Illing and Gauthier, *Physica D* **210**, 180 (2005)]. We found good quantitative agreement of the predicted and the measured bifurcation threshold, bifurcation type and oscillation frequency. Numerical integration of the model yields quasiperiodic and high dimensional chaotic solutions (Lyapunov Dimension  $\sim 13$ ), which match qualitatively the observed device dynamics.

The electronic time-delay feedback device has the potential to generate chaos in the very-high and ultra-high (0.3 - 3 GHz) frequency band. It was built using inexpensive commercially-available components such as ac-coupled amplifiers and a transistor-based nonlinearity, as shown in Fig. 1. We did not neglect, in modeling the device, the fact that RF-components are ac-coupled and we provided a detailed comparison of experimentally observed dynamics and the dynamics of the deterministic model of the device.

In our chaos generator, the complexity of the dynamics was controlled by feedback strength and time-delay, allowing the device to be tuned from steady-state behavior, to periodic, quasi-periodic, and chaotic dynamics. The characteristic time scale of the dynamics could be tuned by adjusting the pass-band characteristics of the feedback loop. We chose to work with feedback characteristics resulting in oscillations of several hundred MHz to a few GHz because this allowed detailed measurements and characterization of the device dynamics. However, the device can, in principle, operate at higher frequencies, such as the 3 - 10 GHz frequency band, by using readily available higher-bandwidth components. The time-delayed feedback is band-pass filtered because, in addition to the cut-off at low frequencies, high frequencies were suppressed due to the finite response time of device components.

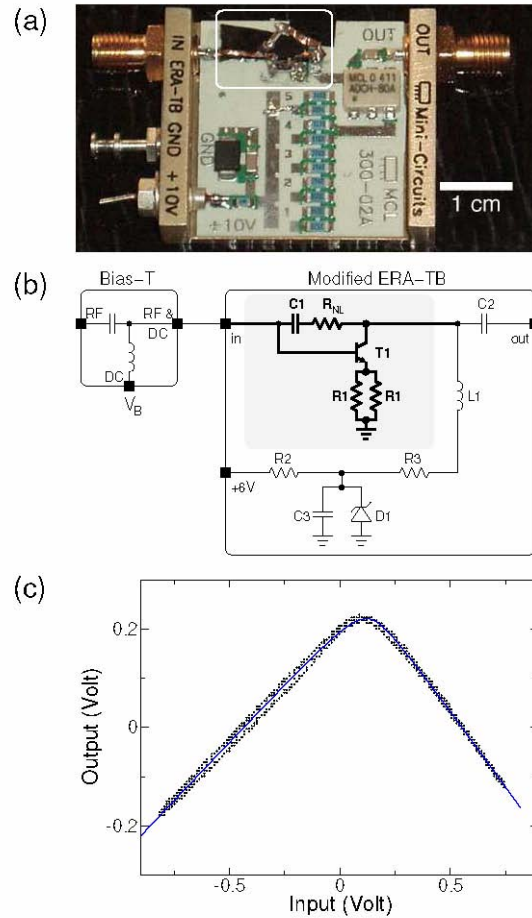


**Figure 1:** Nonlinear element used in the chaotic time-delay electronic device. (a) Modified Mini-Circuits amplifier. (b) Schematic diagram of the circuit with the modified area shown in gray. (c) Observed and predicted nonlinear input-out characteristics of the device.

We compared the measured device dynamics to a simple model of the device consisting of an integro-differential equation with delayed feedback (equivalent to a second-order delay-differential equation). This model captures many of the observed dynamic features. Indeed, good quantitative agreement was found on the level of bifurcations from the steady state and the observed quasi-periodic and chaotic behavior is qualitatively reproduced by the model. In this context, it is important to note that the device was operated in a "weak" feedback regime. In the experimental device, the amplifiers exhibited saturation effects for strong feedback, which introduces additional feedback nonlinearities.

In the strong-feedback regime, we observed chaotic oscillations with a nearly featureless power spectrum. In contrast, the saturation-free model becomes unstable for large values of the feedback parameter. However, omitting saturation effects in the model allowed us to show conclusively that high-dimensional chaos arises in the weak-feedback regime due to the interaction of the linear band-limited time-delayed feedback with the transistor-based nonlinearity.

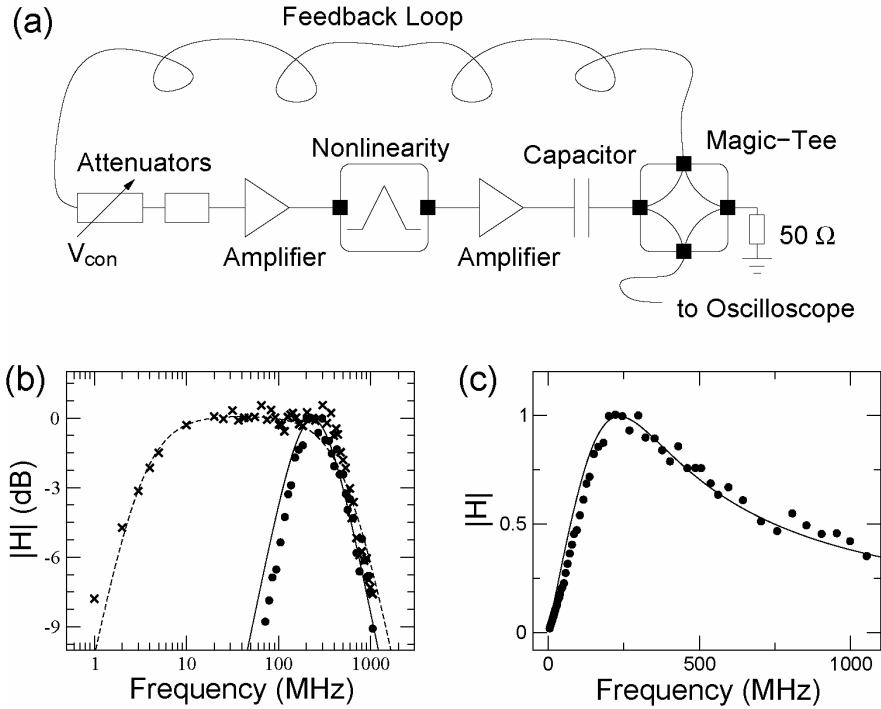


**Figure 2:** Chaotic time-delay electronic device. (a) Schematic layout of the device. (b) Transfer function of the entire circuit with (solid circles) and without (crosses) the presence of a capacitor in the circuit. Lines correspond to a theoretical fit to the data. (c) The transfer-function data with the capacitor shown on a linear scale.

An open question about our observations concerns the high-frequency response of the chaotic oscillator shown in Fig. 2c. The 3dB high-frequency cut-off frequency is around 600 MHz, yet all the components in the loop should have a flat frequency response well beyond 1 GHz (for example, the transistor used in the nonlinear element shown in Fig. 1b has a small-signal bandwidth of 6 GHz).

We found that nonlinear capacitance between the base and emitter and base and collector (the Miller effect) is largely responsible for degrading the bandwidth of the nonlinear element and hence the entire chaotic oscillator. The nonlinear transfer function shown in Fig. 1c was accurate only for low frequencies (the data in the figure was gathered when we injected a 50 MHz sine wave into the nonlinear element). For higher frequencies, there was a substantial phase lag between input and output signals so that the transfer function "opens up."

To understand this effect, we developed a more accurate mathematical model for the nonlinear element that takes into account the Miller effect. We found very good agreement between the experimental observations and theoretical predictions for the nonlinear element at high frequencies using this model. We believe that the bandwidth of the device can be increased by decreasing the resistance of the nonlinear element  $r_{NL}$  and the emitter-to-ground resistance  $r_l$ . We are continuing to explore this possibility. In addition, we are using a data assimilation method recently developed by Rajarshi Roy's group at the University of Maryland for helping us fine-tune the model parameters to improve agreement between theory and experiment.

## I.B. Ultra-high-frequency photonic chaotic elements for sensor networks

We developed and characterized an opto-electronic time-delay oscillator that displayed high-speed chaotic behavior with a flat, broad power spectrum that extended beyond 8 GHz. This chaotic state coexisted with a linearly-stable fixed point, where a finite perturbation or noise with a sufficient amplitude was needed to destabilize fixed point. We found that the fixed point lost stability by the system generating an initially period train of ultrafast pulses, which eventually broke up to generate the chaotic state. We derived an approximate map describing the system that did an excellent job of capturing the observed transient behavior and instability threshold. Our chaotic generator provides a simple device for fundamental studies of time-delay dynamical systems and should be useful as a building block for various ultra-wide-band sensors or sensor networks, such as chaos-based ranging devices, for example.

Our opto-electronic oscillator consisted of a nonlinear element placed in a time-delay feedback loop and displayed a variety of dynamical behaviors that depended on system parameters. As shown in Fig. 3, the beam generated by a semiconductor laser (wavelength 1.55  $\mu\text{m}$ ) was injected into a single-mode optical fiber, passed through a polarization controller, and was injected into a Mach-Zehnder modulator (MZM). The transmission of the MZM was a nonlinear function of the applied voltage (cosine-squared function), as shown in the figure inset, where we independently applied a time-dependent voltage to the radio-frequency (RF) port of the device (half-wave voltage  $V_{\pi,RF}=7.4$  V) and a dc-voltage  $V_B$  to bias it at any point on the transmission curve (half-wave voltage  $V_{\pi,dc}=7.7$  V). Light exiting the modulator passed through an additional piece of single-mode fiber (length  $\sim 5$  m) serving as a delay line and was incident on a photodetector. Half of the resulting signal, denoted by  $V$ , was amplified by an inverting modulator driver (gain  $g_{MD}$ ) and fed back to the MZM via the ac-coupled input port. The modulator driver saturated at high voltage, which we found was well described by a hyperbolic tangent function with saturation voltage  $V_{sat}=9.7$  V. The other half of the signal was directed to a high-speed oscilloscope (8 GHz analog bandwidth, 40 GS/s sampling rate). The total delay of the feedback loop  $T=24.1$  ns.

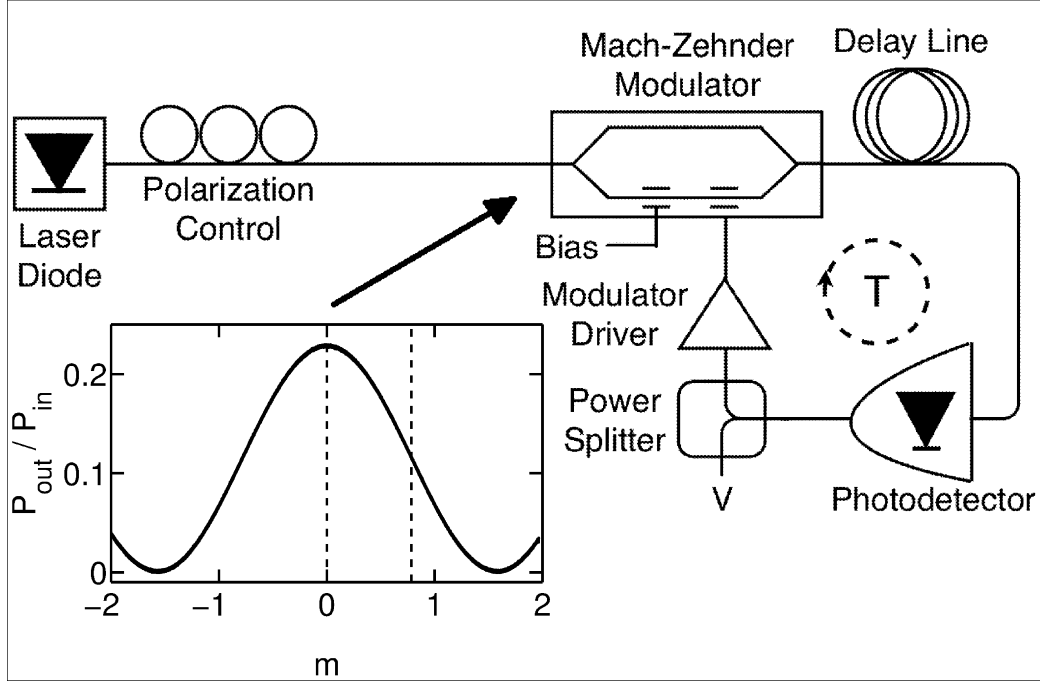


**Figure 3:** Experimental setup. Inset: Nonlinear transmission of the MZM (ratio of the output to input powers of the device) as a function of  $V_B$  specified in terms of the dimensionless parameter  $m$ .

One distinguishing feature of our device was that the amplifier was ac-coupled so that feedback of low frequencies were suppressed. Also, feedback of high frequencies was suppressed due to the finite response time of the photodetector and amplifier. We found that the linear frequency response of the various components of the system was well described by a two-pole bandpass filter with a low- (high-) frequency cut-off  $\omega_- = 1.5 \times 10^5 \text{ s}^{-1}$  ( $\omega_+ = 7.5 \times 10^{10} \text{ s}^{-1}$ ), center frequency  $\omega_0 = (\omega_- \omega_+)^{1/2} = 1.1 \times 10^{10} \text{ s}^{-1}$ , and bandwidth  $\Delta = \omega_+ - \omega_- = 7.5 \times 10^{10} \text{ s}^{-1}$ . A consequence of the bandpass filtering characteristics of our feedback loop was that our system was described in terms of a single time-delay integro-differential equation (or, equivalently, two coupled time-delay differential equations) as opposed to a single time-delay differential equation used by most other research on time-delay electronic or opto-electronic oscillators (see Sec. IA. above).

Another important distinction of our work was that we biased the MZM at the maximum of the transmission curve shown in the inset of Fig. 3 (see the vertical dashed line at  $m = V_B / 2V_{\pi, \text{dc}} = 0$ ). We found that such a bias renders the quiescent state of system linearly stable for all feedback gains in the absence of noise or applied perturbations. Essentially all other research has focused on the case where the bias is set to the half-transmission point of the transmission curve (see the vertical dashed line at  $m = \pi/4$ ), where the quiescent state is most linearly unstable.

Building on our previous work (Sec. I.A.), we found that the dynamics of our opto-electronic oscillator was described mathematically by the following set of dimensionless coupled time-delay differential equations

$$\dot{x}(s) = -x(s) - y(s) + \gamma \cos^2\{m + d \tanh[x(s - \tau)]\} - \gamma \cos^2 m \quad (1)$$

$$\dot{y}(s) = \varepsilon x(s). \quad (2)$$

Here,  $x = g_{MD}V/V_{sat}$ , the overdot denotes the derivative with respect to the dimensionless time  $s = \Delta t$ ,  $\gamma$  is the overall gain of the feedback loop and was proportional the laser power,  $d = V_{sat}/2V_{\pi,RF}$  characterizes the driver saturation,  $\tau = \Delta T$ , and  $\varepsilon = \omega_0^2/\Delta^2$  characterizes the bandpass filter. In our experiments, three of these parameters were held fixed ( $d = 2.1$ ,  $\tau = 1820$ , and  $\varepsilon = 2.0 \times 10^{-6}$ ), while  $\gamma$  ranged from 0-5 by adjusting the laser power with an attenuator and  $m$  ranged from  $-\pi/2$  to  $\pi/2$ .

We found that the fixed points of Eqs. (1) and (2) were located at  $(x^*, y^*) = (0, 0)$ , which is the quiescent state of the oscillator. Stability analysis revealed that the fixed point was stable for small loop gain and, for  $m \neq 0$ , undergoes a Hopf bifurcation (a transition to an oscillatory behavior) at

$$\gamma_H = -\frac{b_{\pm}}{d \sin(2m)}, \quad (3)$$

where  $b_{\pm}$  is a constant that depends on  $\tau$  and  $\varepsilon$  and was approximately equal to  $\pm 1$  for our experimental conditions. By inspection of Eq. (3), we found that  $\gamma_H$  diverges for  $m = 0$ , indicating that the fixed point was linearly-stable for all  $\gamma$ .

We checked this prediction by setting the bias  $m$  with  $\gamma = 0$  and slowly increase  $\gamma$  until the Hopf bifurcation was observed. It is seen in Fig. 4a that there is very good agreement between theory (solid line) and experiment (open boxes) around  $m = \pi/4$  (the standard bias used in most previous experiments), but there is substantial disagreement in the vicinity of  $m = 0$  (see Fig. 4b). At  $m = 0$ , the system lost stability by transitioning directly to a broadband chaotic state at  $\gamma = 4.36$ , as discussed below. Our hypothesis was that the disagreement between our observations and the predictions of Eq. (3) is due to the presence of noise in our system (arising, for example, from laser-power fluctuations due to relaxation oscillations driven by quantum noise, detector dark noise, and detector shot noise).

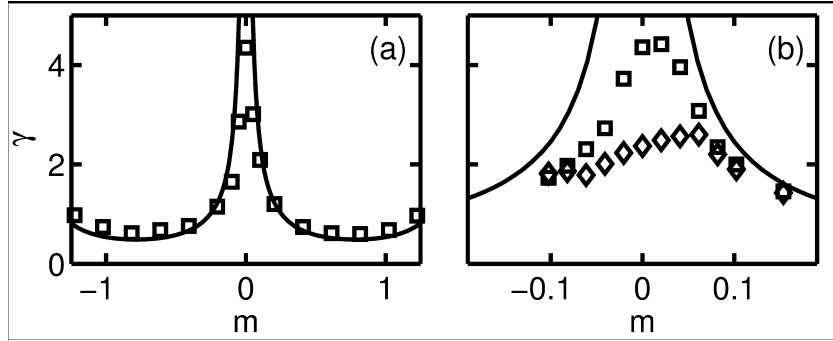


**Figure 4:** The value of  $\gamma$  for which the system transitioned from steady-state to oscillatory behavior as a function of  $m$ , with the Hopf curve superimposed. The squares in (a) and (b) indicate low experimental noise, while the diamonds in (b) indicate a higher level of noise due to the inclusion of the EDFA. Note the good agreement between the theoretical Hopf curve and the experimental data points near  $m=\pi/4$ , whereas near  $m=0$  the discrepancies due to experimental noise become evident.

We added noise to the system to test our hypothesis. Before the laser beam enters the MZM, we inserted an erbium-doped fiber amplifier (EDFA), which amplified and added broadband amplified spontaneous emission noise to the beam, followed by an attenuator so that the total optical power injected into the oscillator was the same. We observed that the fluctuating part of the voltage  $V$  increased by a factor of 2.3 (root-mean-square noise over a bandwidth from dc to 8 GHz) due to the presence of the EDFA. The open diamonds in Fig. 4b indeed show that the instability threshold was decreased due to the increased noise for  $|m|<0.1$ .

When  $m=0$ , we observed that the system lost stability by generating a sequence of ultrashort pulses spaced initially by  $T$  with a pulse duration (full width at half maximum) of  $\sim 200$  ps. To more carefully study this transient behavior, we removed the EDFA, added an additional 3-dB power splitter to the feedback loop, lowered  $\gamma$  so that the system was in the quiescent state and injected 200-ps-long electrical pulses into the loop. For small pulse amplitude, the perturbation decayed. For sufficiently large pulse amplitude, we observed that the perturbation grew rapidly initially, leveled off, and the waveform became more complex, as shown in Fig. 5a. The open triangles shown in Fig. 5b shows the critical value of the pulse amplitude needed to destabilize the fixed point as a function of the feedback loop gain.

We worked with Prof. Eckehard Schöll of the Technical University in Berlin to develop a theory for the pulsing behavior seen in Fig. 5a. By exploring the trajectory in phase space in the presence of a perturbation, we found that it follows the nuclines of Eqs. (1) and (2). By examining how the nuclines shift due to the perturbation, we devised a one-dimensional map that predicted the initial amplitude and timing of the pulses. Furthermore, we found the critical perturbation size needed to destabilize the fixed point. The predictions of the approximate map are shown as solid stars in Fig. 5b, and a full numerical simulation of Eqs. (1) and (2) in the presence of the perturbation is shown as the solid line. Agreement between experiment and both theories is very good.

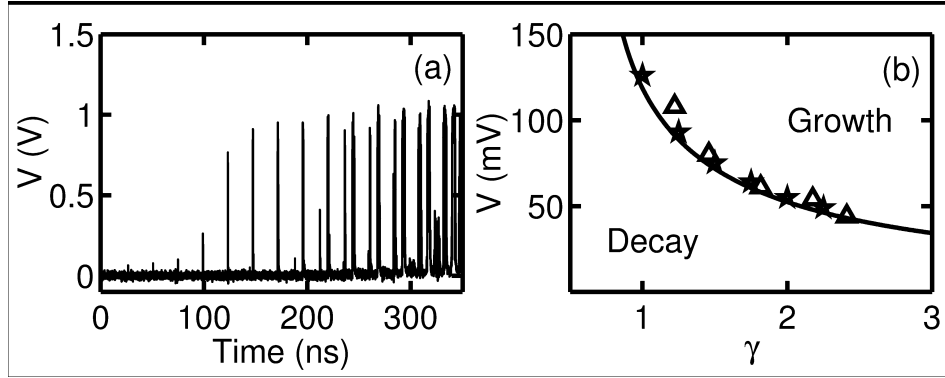


**Figure 5:** (a) The experimental transient behavior that results for  $m=0$  when the system leaves the steady-state. Each pulse has a FWHM  $\sim 0.2$  ns and are separated by the time-delay  $T$ . (b) The critical pulse amplitude as a function of  $\gamma$  in the experiment (triangles) and simulation (stars) with the unstable fixed point of the map (in physical units) superimposed.

In general, transient behavior similar to that shown in Fig. 5a eventually gave way to chaotic behavior as shown in Fig. 6, which is for the case  $m=0$  and  $\gamma=4.80$ , which is just above the noise-induced threshold shown in Fig. 4. Figure 6b shows the one-sided power spectral density (PSD) of the chaotic time series with a resolution bandwidth of 8 MHz. Interestingly, the power spectrum is essentially "featureless" - flat up to the cutoff frequency of the oscilloscope used to measure the dynamics (8 GHz). In greater detail, the spectrum was contained within a range of 15 dB with a standard deviation of 3 dB for frequencies below 8 GHz. Our observation indicated that all frequencies contribute with approximately equal strength and that there are no weakly unstable periodic orbits embedded in the strange attractor. This behavior contrasts with most other chaotic systems where numerous large peaks appear in the power spectrum.

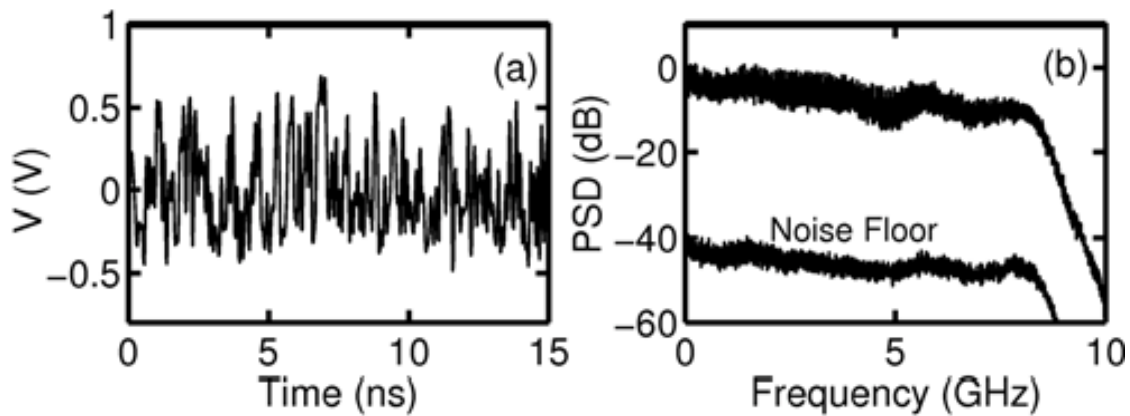


**Figure 6:** The time series (a) and power spectral density (b) of the broadband chaotic behavior in the physical system for  $m=0$  and  $\gamma=4.80$ . The power spectral density of the noise floor obtained for  $m=0$  and  $\gamma=4.30$  is also shown.

We compared our results to the case where  $\gamma=4.30$ , which is just below the threshold for noise-induced instability. As seen in Fig. 6b, the power spectral density is at least 40 dB below that observed when the oscillator was in the broadband chaotic state and was consistent with the noise-floor of the oscillator components and measurement system. Furthermore, the noise floor

was contained within a range of 18 dB with a standard deviation of 2 dB, indicating that the chaotic spectrum was nearly as featureless as the spectrum of the system noise.

Summarizing this part of the program, we developed an opto-electronic oscillator that operated in a regime where the quiescent state was expected to be stable. Through experiments with the physics system and different theoretical approaches, we found that the fixed point was destabilized by a pulsing instability, which caused the system to transition to a coexisting chaotic state. Such an instability and coexisting chaotic state may have important implications for understanding the stability of other time-delay dynamical systems and may find use, for example, in private chaos communication, chaotic LIDAR, and sensor networks consisting of many coupled chaotic elements.

Possible future follow-up work on this project is to explore the dynamics of two or three coupled chaotic devices. It would be important to determine the critical coupling strength where there is a measurable change in the dynamics of one oscillator due to the presence of other oscillators, and whether synchronization, possibly with a time lag, can be observed.

## **II. Ultra-low-light-level all-optical switching using optical patterns**

Just before the start of this project, we discovered a novel approach for achieving ultra-low-light-level all optical switching. This approach involves combining near-resonance, sub-Doppler nonlinear optics with optical pattern formation. In particular, we observed that patterns generated by a counterpropagating-beam instability can be switched with a pulse of light that has less than 3,000 photons. During the course of this project, we have performed a detailed study of the switch, optimized its behavior, and developed a theoretical model that describes its operating characteristics. Section II.A. describes the main focus of this work, where we used a rubidium vapor cell as the nonlinear material. We have been concerned that Doppler broadening of the resonance causes some background absorption, so we have also developed an anisotropic trap for ultra-cold rubidium atoms that will be used for future research on all-optical switching. This work is described in Sec. II.B.

### **II.A. Patterns and switching using a vapor cell as the nonlinear medium**

We briefly describe our approach for all-optical switching, pointing out what we found to be the most important experimental parameters to optimize the switch behavior. A diagram of the atomic-vapor experimental setup is shown in Fig. 7. Two beams of light from a common laser source counterpropagated through warm rubidium vapor contained in a glass cell. The light source was a frequency-stabilized cw Ti:Sapphire laser, the output of which was spatially filtered using a single-mode optical fiber with an angled entrance face and a flat-polished exit face. The beam was then collimated using a pair of convex lenses arranged as a telescope. The spot size ( $1/e$  field radius), denoted by  $w_0$ , was controlled by the configuration of the telescope, and the beam waist was located in the center of the vapor cell. The power ratio between the pump beams was controlled by a half-wave plate at the input of the first polarizing beam splitter (PBS1). We denote the beam passing through PBS1 as the forward beam and the reflected beam as the backward beam. A second half-wave plate in the backward beam path rotated the polarization such that the pump beams are linearly polarized with parallel polarizations.

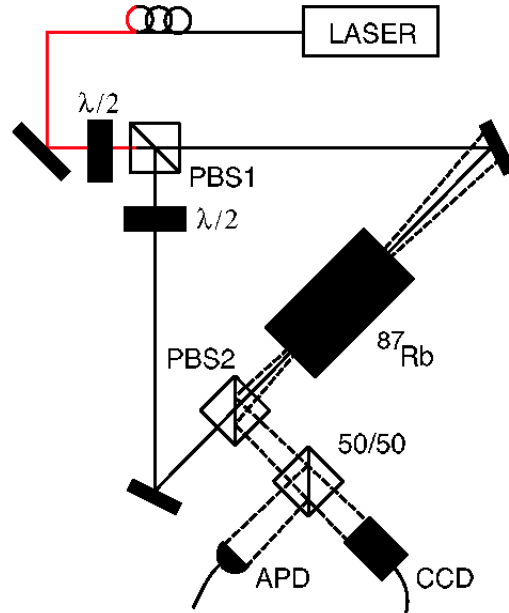


**Figure 7:** Experimental setup for transverse optical pattern generation. The output of a frequency-stabilized cw Ti:Sapphire laser serves as the source. A polarizing beamsplitter (PBS1) separates the forward (cw) and backward (ccw) beams within the triangular ring cavity. The backward beam is brought into horizontal polarization by a half-wave plate ( $\lambda/2$ ). The forward and backward beams counterpropagate through a warm  $^{87}\text{Rb}$  vapor contained in a 5-cm-long glass cell. A polarizing beam-splitter (PBS2) reflects instability-generated light in the vertical polarization which is observed by a CCD camera and avalanche photodiode (APD).

The cell has length  $L=5$  cm and diameter 2 cm. The rubidium contained in the cell was not isotopically enriched and thus contained the two naturally abundant isotopes: 72%  $^{85}\text{Rb}$ , 28%  $^{87}\text{Rb}$ . The cell was heated to 80 °C corresponding to an atomic number density for  $^{87}\text{Rb}$  of  $2 \times 10^{11}$  atoms/cm<sup>3</sup>. The cell had uncoated optical-quality quartz windows that had fixed and opposing tilt angles of  $\pm 11$  degrees with respect to the incident laser beams to prevent possible oscillation between the windows. The cell had no paraffin coating on the interior walls that would prevent depolarization of the ground-state coherence, nor did it contain a buffer gas that would slow diffusion of atoms out of the pump laser beams. The Doppler-broadened linewidth of the transition at this temperature was  $\sim 550$  MHz. To prevent the occurrence of magnetically-induced instabilities and reduce Faraday rotation, a cylindrical  $\mu$ -metal shield surrounded the cell and attenuated the ambient magnetic fields by a factor of  $>10^3$ . In order to attenuate the static magnetic field created by the heaters coils, they were placed outside the shielding. We found that the most important changes to our setup (in order of importance) was using a vapor cell with optical quality windows that were angled, shielding the ambient magnetic field, spatially filtering the pump beams, and determining the optimum pump beam diameter in the cell.

In the context of all-optical switching, pattern formation was the most notable feature of the counterpropagating beam instability described above. When the pump beams were above threshold, *i.e.*, had total power greater than 420  $\mu\text{W}$ , generated light was emitted at an angle  $\sim 4$  mrad to the pump beam axis as shown in Fig. 8a and can be understood as arising from

competition between two different nonlinear processes: backward four-wave mixing in the phase-conjugation geometry and forward four-wave mixing. A perfectly symmetric system was expected to generate light with intensity that is distributed evenly around the azimuthal angle, and hence would form a ring pattern in the far field. Perfect symmetry, however, is unattainable in the laboratory where imperfections in optical elements impart small perturbations on the phase and amplitude of the beams. The instability responded to such perturbations by generating patterns that are not cylindrically symmetric. For this reason, the most common patterns reported consist of two, four, or six spots in a variety of arrangements. In all cases, the spots were located along the ring projected by the cones onto the detection plane as illustrated in Fig. 8b-d.

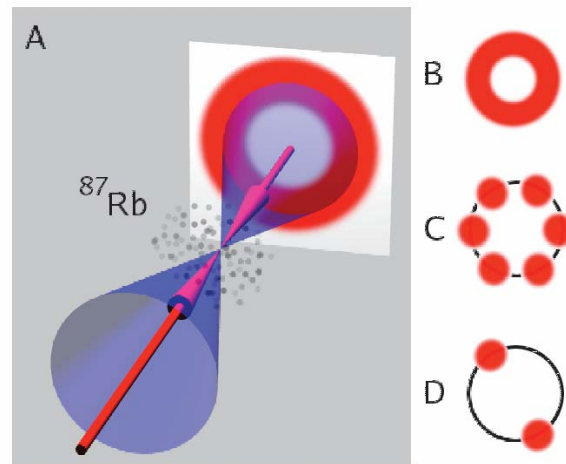


**Figure 8:** When pump beams (red) of a sufficient intensity counterpropagate through warm rubidium vapor, light is generated along cones (blue) centered on the pump-beam axis. A far-field detection plane shows patterns formed by the generated light. b) A ring pattern is expected for a perfectly symmetric system. c) Six spots form a hexagon, the typical pattern for pump beam powers more than 20% above threshold. d) Two spots are observed just above threshold or when the pump beams are mis-aligned.

We found that the azimuthal angle of the instability-generated beams was extremely sensitive to perturbations because the symmetry breaking of our setup is small. The preferred azimuthal orientation of the pattern could be overcome by injecting a weak switching beam along the cone of emission at a different azimuth. Typically, this caused the pattern to rotate such that one spot is aligned to the switching beam with essentially no change in the total power of the pattern.

### *Switch response*

In the following sub-sections, we summarize our best switching results obtained to date.

To quantify the dynamic behavior of the switch, we injected a series of pulses by turning the switch beam on and off with the EOM. Spatially filtering the output pattern enabled us to directly measure the switch behavior. High-contrast switching was confirmed by simultaneously measuring two output ports. Figure 9a shows the power of the injected switch beam as a function of time. The signal from the off-state detector is shown in Fig. 9b and is high

when the switch beam was not applied and low during a switch-beam pulse. The on-state detector is shown in Fig. 9c and shows the opposite behavior, it was low when the switch beam was not applied and high during each switch-beam pulse. These alternating signals demonstrate switching of the power from one switch state to another with high contrast. The total power generated in the pattern is  $\sim 3 \mu\text{W}$ . Each aperture selected one of the two generated spots, so the switch output power was  $\sim 1.5 \mu\text{W}$  per aperture.

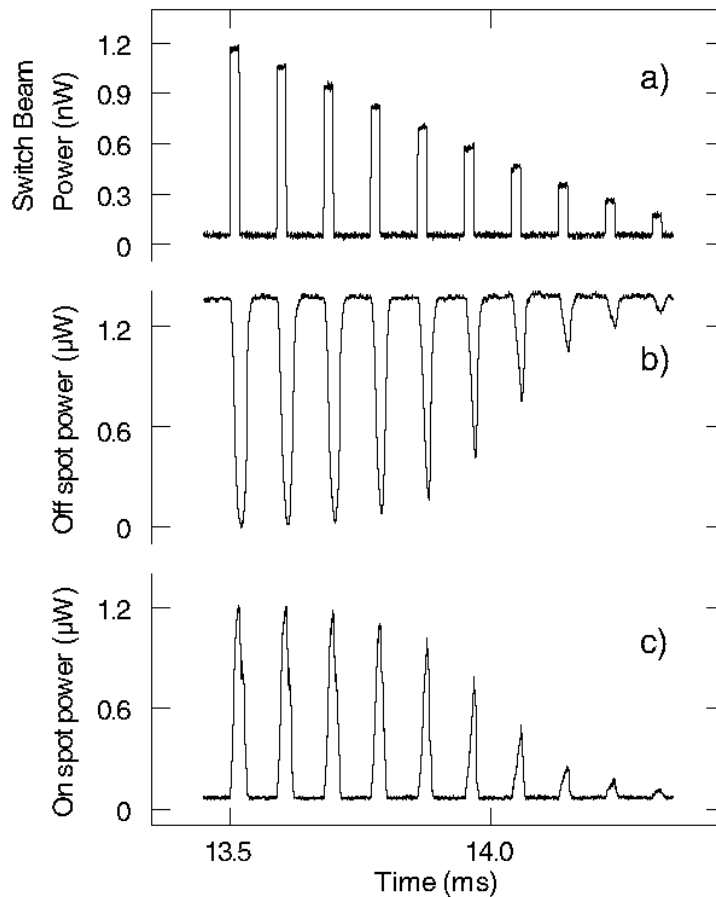


**Figure 9:** The switch responds to a series of ten pulses by transferring power from the off state spots to the on state spots. a) The switch beam power steadily decreases in power from 1.2 nW to 200 pW. b) The off spot is extinguished in the presence of the switch beam. c) The on spot power increases in the presence of the switch beam. The data shown are collected in a single shot that contains 22 additional ten-pulse sets with similar response. No signal averaging has been performed on the switch response data (b,c) the measured switch-beam power shown in (a) is averaged over 10 shots.

One notable feature of the system response is the transition from complete switching to partial switching. The first three pulses in Fig. 9 show that the on-state detector was fully illuminated and the off-state detector was dark. This indicates that the switch beam caused complete rotation of the pattern and transferred all of the power from the off-state spots to the on-state spots. For the last seven pulses in the series, the system exhibited partial switching, where the on-state detector was partially illuminated and the off-state detector was partially darkened. This partial

response indicates that the off-state spots are suppressed but not extinguished when the switch beam was applied with less than 900 pW. Similarly, the on-state spots were generated but not at full power. In this intermediate regime, from 900 pW to <300 pW, the response depended on the input power.

### Switching photon number

To quantify the sensitivity of the system, we measured the response time and calculate the number of photons  $N_p$  required to actuate the switch. The response time of the device  $\tau_r$  is defined as the time between the initial rising edge of the electronic signal driving the EOM and the point where the on-spot signal crosses a threshold level set to roughly correspond to a signal-to-noise ratio of  $\sim 3$  dB. (The SNR  $\sim 3$  dB criterion corresponds to the threshold where the bit-error-rate decreases below 0.05, *i.e.*, it is the point where pulses can be correctly detected with probability greater than 5%.) Results using this threshold are shown in Fig. 10a. We found that the measured response time increases as the input switch beam power decreases.

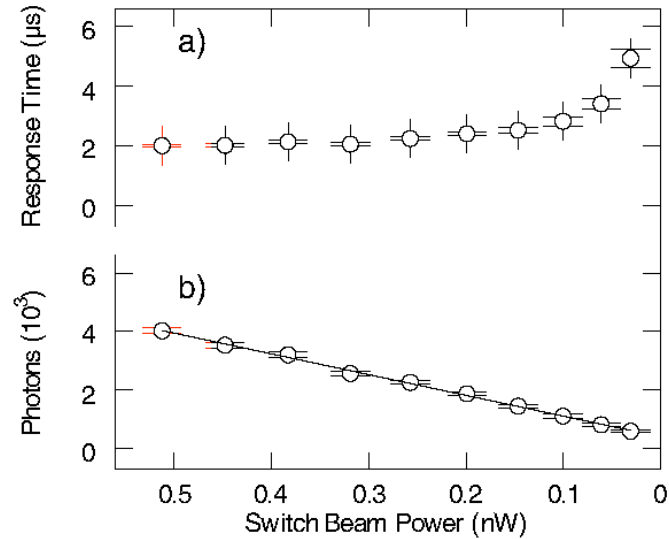


**Figure 10:** The response time  $\tau_r$  and number of switching photons  $N_p$  as a function of input power. Data are generated from 22 sequential traces like the one shown in Fig. 9 acquired after a single trigger. The error bars indicate one standard deviation of the measured values. The solid line indicates the fit:  $N_p = 7081 P_s + 404$  for  $P_s$  in nW.

The number of photons required to actuate the switch was given by  $N_p = \tau_r P_s / E_p$  where  $\tau_r$  is the response time,  $P_s$  is the switch beam power and  $E_p = 2.54 \times 10^{-19}$  J is the photon energy. For ten switch-beam powers between 510 pW and 35 pW, the response time is plotted in Fig. 10a, and the number of switching photons is plotted in Fig. 10b. The response time is longer for weak switch-beam powers so the photon number decreases gradually as the input power decreases. The data points indicate the average of 22 data points for each of the ten switch-beam pulses, and the error bars represent one standard deviation in the response times observed for each pulse.

The implication of the linear regression shown in Fig. 10b is that, in the limit as  $P_s \rightarrow 0$ , the number of switching photons  $N_p$  asymptotes to a finite minimum. This would indicate that the minimum number of photons capable of actuating the switch is roughly 400. The final data point shown correspond to switching with  $N_p = 600 \pm 40$ , only 200 photons above this limit, and a factor of  $\sim 5$  lower than the first reported observation of pattern-based all-optical switching with 2,700 photons that we obtained before this program was initiated.

### *Transistor-like response*

The response shown in Fig. 9, demonstrating the saturated and linear response regimes, suggested that this device operated in a manner that is analogous to an electronic transistor. Furthermore, the two response regimes exhibited by the switch indicated that the output satisfies the conditions for signal level restoration.

For a device to exhibit signal level restoration, variations in the input level cannot cause variations in the output level. In every device, however, there is a narrow range of input levels, known as the intermediate region, that lead to intermediate output levels. For input levels above or below the intermediate range the output is saturated as a logic high or low, respectively. In the case of the Rb-vapor device, this intermediate region was between 900 pW and  $< 35$  pW. For input levels above 900 pW, the output was high with a level set by the pump beam power.

Signal level restoration is a key property of the electronic transistor enabling large networks of electronic logic elements. This demonstration of an optical logic element that exhibits level restoration is a key step towards practical optical switches. An all-optical transistor would have applications in many data processing and communication networks in the future.

### *Theoretical Model of the Pattern-Based Switch*

In order to establish the necessary ingredients for a theoretical model to describe the switching behavior observed experimentally, we developed a simple extension to a previous model of a pattern-forming counterpropagating beam system based on the model of Firth and Paré. We extend this prior work by simulating all-optical switching with transverse patterns. Specifically, we simulated the effect of a weak switch beam on the orientation of the hexagonal pattern generated by gaussian pump beams that counterpropagate through a Kerr-type nonlinear medium. Simulations of the time response of this system show behavior that is qualitatively similar to experimental observations. In particular, the response time increases as the switch-beam power decreases.

The model used describes the propagation of the waves in all three dimensions (along the beam propagation direction as well as two transverse dimensions). We assumed scalar fields, *i.e.* the model did not account for the vector nature of the fields, and hence could not describe polarization instabilities, and we did not include absorption effects. Nonetheless, this model was sufficient to describe pattern formation in counterpropagating-beam nonlinear optical systems. The forward and backward fields counterpropagating through a Kerr-like medium are described by the dimensionless equations

$$\left(\frac{\partial}{\partial z} + \frac{\partial}{\partial t}\right)F = \frac{i}{4\pi f} \nabla_{\perp}^2 F + i(|F|^2 + 2|B|^2)F, \quad (4)$$

$$\left(-\frac{\partial}{\partial z} + \frac{\partial}{\partial t}\right)B = \frac{i}{4\pi f} \nabla_{\perp}^2 B + i(|B|^2 + 2|F|^2)B. \quad (5)$$

Here, time is normalized by the transit time through the medium,  $t_r = nL/c$ , the longitudinal dimension  $z$  is normalized by the medium length  $L$ , and the transverse dimensions  $x, y$  are normalized by the beam waist where  $f$  is the Fresnel number, and  $F$  ( $B$ ) is the forward (backward) field amplitude. The nonlinear coefficient is scaled into the field amplitudes and is assumed to be positive as appropriate for our experimental conditions. The medium length is also scaled into the field amplitudes such that  $F^2 = IL$ , where  $I$  is the pump-beam intensity.

Equations (4) and (5) are solved numerically using a split-step beam propagation method where linear diffraction is computed via fast Fourier transform. We used a numerical grid of  $256 \times 256$  transverse points and 20 longitudinal slices. The numerical grid was slightly rectangular with the  $x$  dimension 1% larger than the  $y$  dimension to prevent the square symmetry of the grid from biasing the pattern formation process. Additionally, suitable choice of parameters and appropriate spatial filtering are used in order to avoid spurious high transverse wavenumber instabilities.

We conducted simulations with a wide range of values of  $f$  between 64 and 4, where our experimental conditions correspond to  $f=5.3$ . Simulations in this range all exhibit hexagonal pattern formation. In order to simulate the specific geometry of our experiment, the results shown here are of simulations where  $f=5.3$  and  $IL=0.565$  (~25% above threshold). Images of the far field pattern generated in a typical simulation are shown in Fig. 11A, where the time corresponding to each frame is indicated in units of the transit time  $t_r$ . In the initial frame of Fig. 11A, the transmitted forward pump-beam is visible at the center, and the weak off-axis perturbation is visible to the right. This perturbation is used to quickly induce hexagonal pattern formation. Without the initial perturbation, hexagons are spontaneously generated after 100-150 transit times. At  $t=17$ , the field that is conjugate to the perturbation, and due to forward four-wave mixing, is visible to the left of the central pump. The dark dot in the center of the first two frames is the result of numerical filtering used to remove the DC artifact introduced by computing the far-field via FFT. This filtering is only performed on the images in order to improve the contrast, and not during the simulation itself. At  $t=23$ , a ring pattern has formed that is replaced by hexagons at  $t=53$ . The seed beam is turned off at  $t=35$  and is not visible at  $t=53$ . The second row of frames shown in Fig. 11A are collected after the application of an off-axis switch-beam, which turns on at  $t=85$ .

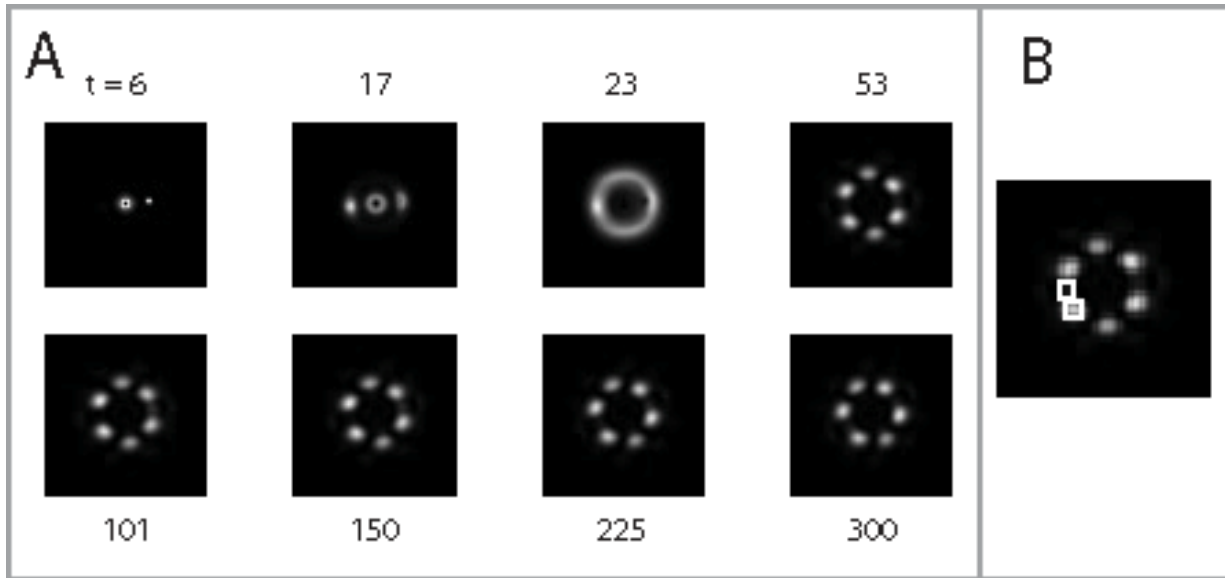


**Figure 11:** Numerical simulation of counterpropagating Gaussian beams shows ring and hexagon pattern formation in the far field. (A) For this case, the pump beams are perfectly counter-propagating. (B) The location of the on- and off-state apertures are indicated relative to the initial hexagon pattern that forms at  $t=53$ . The on-state aperture (upper square) is located opposite the applied switch beam, and the off-state aperture (lower square) transmits the spot immediately counter-clockwise from the on-state aperture.

In our simulations, we observed that injecting a weak switch beam into the nonlinear medium after hexagons have formed causes the hexagon pattern to rotate such that a bright spot is aligned to the direction of the switch beam. This rotation is illustrated in the lower four frames of Fig. 11A. The switch beam is applied at  $t=85$ , and becomes visible between the two right-side spots at  $t=101$ . At  $t=150$ , the counterclockwise rotation of the pattern can be observed and continues until the end of the simulation at  $t=300$  where the pattern has rotated such that the locations that were previously bright are now dark.

As in the experiments, the patterns generated in this simulation can be spatially filtered in order to define two or more output channels. Figure 11B indicates the location of the apertures used to filter the numerical results. The power transmitted by these apertures was calculated by summing the simulated intensity values within each aperture.

After the initial transients in the pattern formation, the power in the off- and on-spots stabilized within 50 transit times. At  $t=85$ , the switch-beam was applied and the pattern begins to rotate, transferring power from the off-state aperture to the on-state aperture. Complete rotation occurred within 200 transit times. For lower switch beam power, the pattern rotated more slowly. To compare the change in response time observed in the simulation to that observed experimentally, we measure the response time of the simulated switch as the time between the application of the switch beam ( $t=85$ ) and the threshold crossing for the on-spot. The threshold was chosen to roughly correspond to the threshold level used in the experiments.

The response time of the simulated switch data ranges from 40 transit times to 210 transit times, as shown in Fig. 12. For comparison, the transit time of the 5-cm-long vapor cell used in our

experiment is 160 ps, so the simulated response times would correspond to experimental values of 6.4 ns and 33.6 ns respectively. Experiments observe response times between 2 and 4  $\mu\text{s}$  in Rb vapor, so it is clear that this numerical model does not agree quantitatively with these observations. However, the simulated response time does exhibit a sharp increase in the limit of low switch-beam power, which is qualitatively similar to experimental observations. This increase in response time for weak inputs may be an indication that the switch undergoes critical slowing down, which would not be surprising since the orientation of the pattern exhibits multi-stability between the preferred orientations.

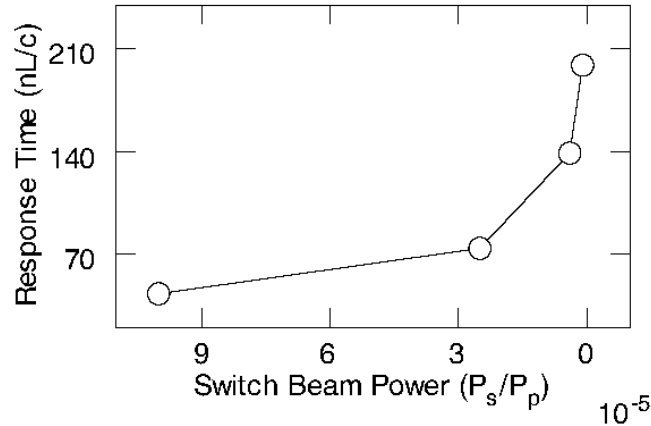


**Figure 12:** Simulation of the switch exhibits an increase in response time for decreasing power that is qualitatively similar to experimental observations. To facilitate comparison to Fig. 10a, the horizontal axis has high switch-beam power to the left and low switch-beam power to the right.

Another notable feature of these numerical results is that, despite the limitations of the model, the amount of switch-beam power, relative to the total pump power, required to rotate the pattern is of the same order of magnitude as what has been observed experimentally. Therefore, the sensitivity demonstrated in experimental work is largely described by this model.

## II.B. 2D-MOT for all-optical switching using optical patterns

During this project, we have designed and constructed an anisotropic (nearly one dimensional) Magneto-Optical Trap (MOT).

We believe that any effect that raises the threshold for the pattern forming instability also raises the number of switching photons. Schäpers *et al.* have identified grating washout (due to wavelength-scale motion of the atoms) as an effect that raises the threshold for the pattern-forming instability. We also believe that residual absorption from off-resonance Doppler-shifted atoms raises the number of switching photons. These deleterious effects can be removed using a sample of cold atoms, an approach taken by the other groups studying EIT-based switching. One open question is whether it is possible to observe transverse optical patterns in cold atoms driven by counterpropagating laser beams. We believe that research on optical pattern forming using cold atoms will be advanced more readily using a trap that can achieve a greater optical depth than has been used in these previous studies such as the highly anisotropic MOT (A-MOT) pioneered by Mara Prentiss' group.

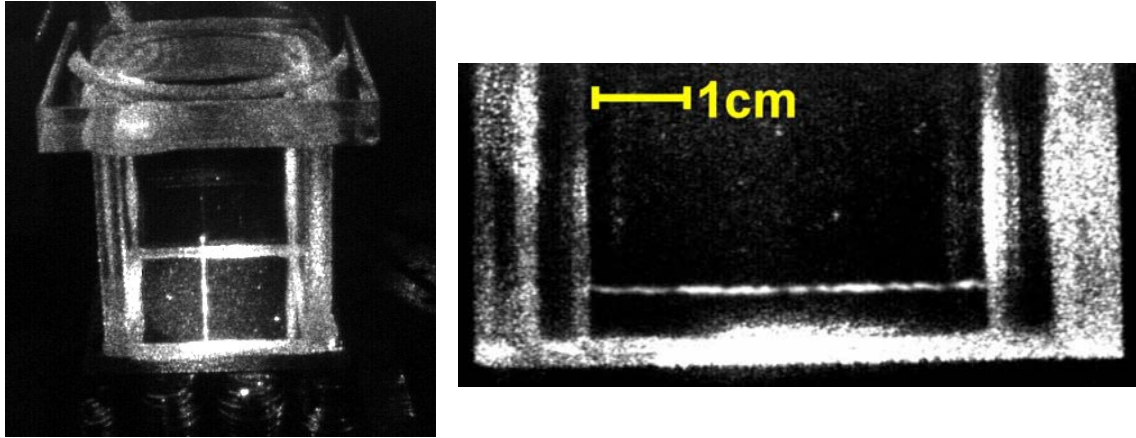


**Figure 13:** Top and side view of 2-D MOT imaged with a CCD camera. The elongated atom-cloud's length was limited mainly by the extent of the cell.

We constructed such an A-MOT (see Figure 13) with an length-to-radius aspect ratio of the trapped atom cloud of 100:1. This trap has a high optical depths along the long dimension of the trap of  $OD=60$  (meaning a transmission of  $e^{-60}$ ) while maintaining low optical depths transverse to this direction. It allows using any state of polarization for the laser beam propagating along the long dimension of the trap as well as imposing an arbitrary homogenous magnetic field along the long dimension of the trap. We measured large amplifying resonances due to atomic recoil with a gain of 1,500% relative to the input power. This is an indication of strong nonlinear interactions between the atoms and the light and also implies possible spatial self-organization of the atom cloud, which could further enhance nonlinear effects.

In the future, we intend to use this system for substantially increasing nonlinear interaction strengths, thereby allow us to investigate pattern formation and all-optical switching. Another advantage of this type of trap is the possibility of an atom chip realization of the trap, opening a pathway toward system-on-a-chip integration.